

Weyl Metal Phase in Delafossite Oxide

PtNiO₂

Gang Bahadur Acharya^{1,2†}, Mohan Bikram Neupane^{1†}, Rojila Ghimire¹, and
Madhav Prasad Ghimire^{1*}

¹*Central Department of Physics, Tribhuvan University, Kirtipur, 44613, Kathmandu, Nepal*

²*Leibniz IFW-Dresden, Helmholtzstr. 20, D-01069 Dresden, Germany*

E-mail: madhav.ghimire@cdp.tu.edu.np

Abstract

On the basis of density functional theory calculations we predict Weyl points in rhombohedral structure of PtNiO₂ having symmorphic symmetry. From the formation energy and phonon calculations, PtNiO₂ is found to be structurally stable. The magnetic ground state is ferromagnetic with an effective magnetic moment of 1.01 μ_B per unit cell. The electronic structure shows major contributions from Pt-5d, Ni-3d and O-2p orbitals with band crossing close to the Fermi level. The orbital contribution around 8 eV above the Fermi level are from the Pt-s, p orbitals forming a hidden kagome-like electronic structure confirmed by surface Fermi surface spectral function. We found 20 pairs of confirmed Weyl nodes along the magnetic easy axis [100]. These results are expected to provide a useful and exciting platform for exploring and understanding the magnetic Weyl physics in delafossites.

^{1†} These authors contributed equally to this work.

Introduction

Materials with unusual quantum phenomena, such as unique transport features and topological surface states, topological semimetals, etc. have generated lots of interest in recent years.¹ In electronic band structures of topological semimetals, the interaction of symmetry and band topology is important. As a result, topologically protected zero-dimensional point-like or one-dimensional line-like Fermi surfaces in momentum space are formed.² Topological semimetals emphasize various forms of low-energy excitations near the protected band-crossing points, such as Dirac fermions,^{3,4} Weyl fermions,⁵⁻⁹ nodal line fermions,¹⁰ and triple fermions,^{11,12} under various symmetries in the crystals. Weyl semimetals (WSMs) significate at extension since both the conduction and valence bands cross each other near the Fermi level (E_F), and the crossing points, known as Weyl points (WPs), appear as monopoles of Berry curvature in the momentum space. WPs have a definite chirality +1 or -1. The Berry curvature is a magnetic field in the momentum space that causes anomalous velocity of electron motion in real space. As a result, Weyl monopoles play an important role in electrical conduction, such as in the anomalous Hall effect. WPs location and their energies are significantly influenced by magnetic order as well as spin structures.¹³ Using spectroscopic and electrical transport approaches, many WSMs have already been identified theoretically and confirmed experimentally.¹ The majority of these compounds are nonmagnetic, therefore achieving WPs require the presence of a non-centrosymmetric crystal structure. Nonmagnetic WSMs have lots of charge carrier mobility and a significant magnetoresistance.^{14,15} If the compound is magnetic, the WPs can appear even in centrosymmetric structures.¹⁶ Magnetic WSMs have recently attracted attention as a new platform for exploring the interaction of chirality, magnetism and topological order. These studies potentially lead to novel quantum states, spin-polarized chiral transport,¹⁷ and unusual optical features.¹⁸⁻²⁰ Compared with the non-magnetic WSMs, magnetic WSMs gives us a powerful tool for manipulating band structure and associated electromagnetic performance. Magnetic arrangement breaks the time reversal symmetry in magnetic WSMs, requiring additional symme-

try to protect the topological property. Pyrochlore iridate $\text{Re}_2\text{Ir}_2\text{O}_7$ (Re=rare earth)⁵ and HgCr_2Se_4 ,⁶ for example, are the first magnetic topological WSMs proposed, and they have several pairs of time-reversal-symmetry-breaking Weyl nodes. A half-metallic ferromagnet $\text{Co}_3\text{Sn}_2\text{S}_2$,^{21–24} is also predicted as magnetic WSM which contains only six WPs above E_F . From density functional theory (DFT) calculations and using angle-resolved photoemission spectroscopy experimentally, WSMs were found. In magnetic WSMs, there are possibilities for the creation, annihilation and shifting of WPs due to the effect of magnetization rotation.²⁴ Also, Co_2MnGa ,^{25,26} Co_2MnAl ,²⁷ $\text{Mn}_3\text{Sn}/\text{Mn}_3\text{Ge}$,^{28,29} GdPtBi ³⁰ and YbMnBi_2 ³¹ are demonstrated as magnetic WSMs.

After 1997, the delafossite structural series of oxides ABO_2 , where (A=Pt, Pd, Ag and Cu and B=Cr, Co, Fe and Ni)^{32–35} have been studied due to the transparent conductive property found in Cu based delafossites.³⁵ Likewise, Pt and Pd based delafossites having d^9 configuration possess high conductivity, comparable to that of Cu and Ag.³⁶ In search of PtCoO_2 's high conductivity, it was reported that $6s$ and $6p_x/p_y$ and $d_{3z^2-r^2} + d_{xy}/d_{x^2-y^2}$ orbitals of Pt formed hidden kagome-like features.³⁷ PdCoO_2 's high mobility was also compared to that of NbAs (a Weyl semimetal),³⁸ implying that metallic delafossites can be an alternative to today's semi-conducting devices. But, hitherto topological features of delafossite structures are not investigated. Thus, our work paves a pathway for the realization of Weyl features in the magnetic delafossites which has never been explored. Our particular interest is in searching for the topological Weyl properties in delafossite structural oxide PtNiO_2 .

By means of DFT calculations, we show that ferromagnetic delafossite oxide PtNiO_2 is a magnetic WSM. The electronic, magnetic and Weyl characteristics of delafossite oxide PtNiO_2 are investigated. The gap between the conduction and valence band opens due to the effect of spin orbit coupling (SOC), resulting in topological bulk Weyl properties as well as its surface properties. Along the $[100]$ magnetic easy axis, we found total of 40 Weyl points. The proximity of all the WPs to E_F suggests the possibility of transport experiments. Our findings provide an excellent material for additional experimental synthesis and

investigations of time-reversal breaking ferromagnetic WSMs.

Methods

We performed DFT calculations to investigate the electronic properties of PtNiO_2 using the full-potential local orbital code (FPLO),³⁹ version 18.00-52, with a localized atomic basis and full potential treatment. The exchange-correlation energy functional used is the generalized gradient approximation in the parameterization of Perdew, Burke, and Ernzerhof's (PBE - 96).⁴⁰ Using the PYFPLO module of the FPLO tool,³⁹ we extract the Wannier tight-binding Hamiltonian by projecting Bloch states over atomic orbital-like Wannier functions for further analysis of the electronic structure. The localized Wannier basis states include Pt $[5d, 6s]$, Ni $[3d, 4s]$, and O $[2s, 2p]$ orbitals. The Wannier model is converged in the Brillouin zone (BZ) with a $12 \times 12 \times 12$ grid sample. These Wannier Hamiltonians are then used to investigate the Weyl properties along various magnetization directions, as well as associated topological aspects including surface attributes. The energy convergence criterion was chosen at 10^{-6} Hartree. Dynamical stability has been studied using density functional perturbation theory (DFPT) implemented in quantum espresso code.⁴¹ Broyden-Fletcher-Goldfarb-Shanno (BFGS) method has been used to perform ground-state optimization. The pseudopotential used is non-conserving type. The plane-wave basis set cut off energy chosen is 95 Ry. For Brillouin zone integration $12 \times 12 \times 2$ k mesh was taken. The Kohn-Sham equation is solved using the iterative Davidson-type diagonalization approach with an energy convergence threshold of 10^{-10} Ry. We have used $4 \times 4 \times 1$ q mesh which calculates the phonon at any wave vector. The surface states in the projected two-dimensional (2D) BZ were obtained from the surface Greens function of the semi-infinite system.⁴²

Results and discussion

Crystal structures

PtNiO₂ belongs to a trigonal system of hexagonal crystal family with space group $R\bar{3}m$ (no. 166).⁴³ The structure is quasi two dimensional with lattice parameters $a = b = 2.92 \text{ \AA}$, $c = 18.24 \text{ \AA}$ and angles $\alpha = \beta = 90^\circ$ and $\gamma = 120^\circ$. Platinum cation is linearly bonded with two oxygen anions. Nickel forms octahedron with oxygen. This delafossite comprises of Pt layer stacked between NiO₆ octahedra. The point group is $\bar{3}$ or D_{3d} . It is a symmorphic system with inversion center. In order to examine the stability of PtNiO₂, the formation energy was

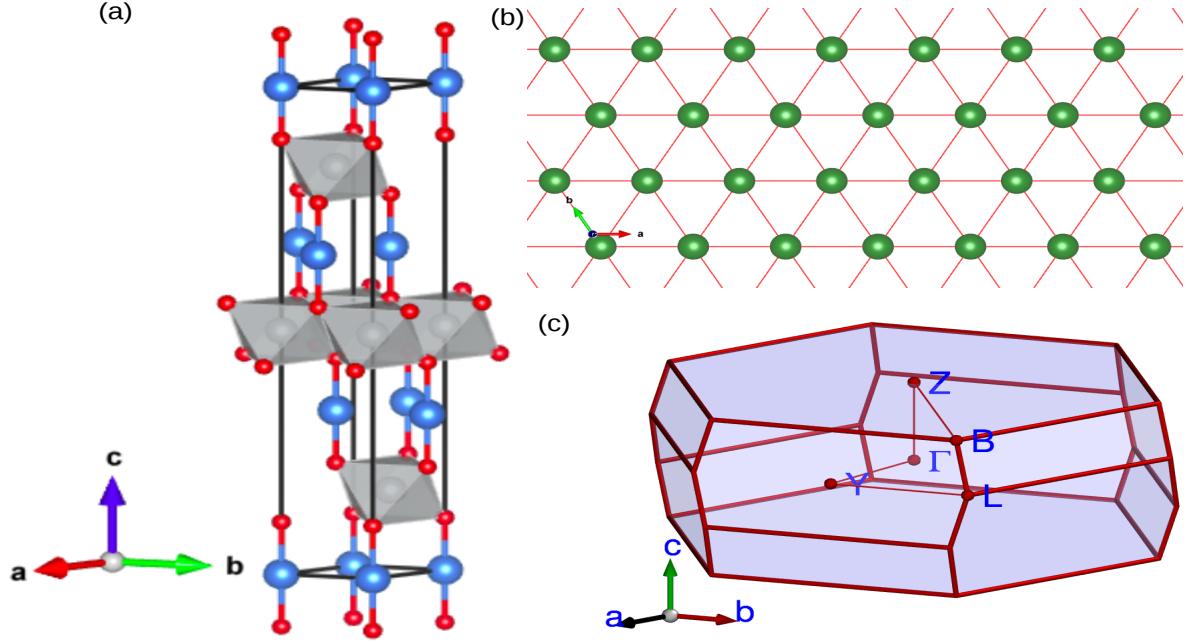


Figure 1: (a) Crystal structure of PtNiO₂ (blue, red and silver balls represent Pt, O, and Ni atoms respectively, octahedral arrangement between Ni and O atoms); (b) The triangular lattice of Ni atoms in a-b plane and (c) Bulk BZ. The red dots and lines indicate the high-symmetry points and paths respectively in the BZ.

calculated using given equation:

$$E_{For} = E_{PtNiO_2}^{Tot} - [E_{Ni}^{bulk} + E_{Pt}^{bulk} + 2E_O^{bulk}] \quad (1)$$

where $E_{PtNiO_2}^{Tot}$ indicates the total energy of the crystal. E_{Ni}^{bulk} , E_{Pt}^{bulk} , and E_O^{bulk} are the total energies of nickel, platinum and oxygen atoms respectively obtained from the bulk energy calculations. The formation energy per atom is -0.58 eV. The negative value of formation energy shows the thermodynamical stability of PtNiO₂.

The calculated phonon dispersion curve is shown in Fig. 2. The unit cell contains 12 atoms, resulting in 36 phonon dispersion modes with three acoustic and remaining optical branches. The partial phonon density of states are presented in Fig. 2 which depicts the

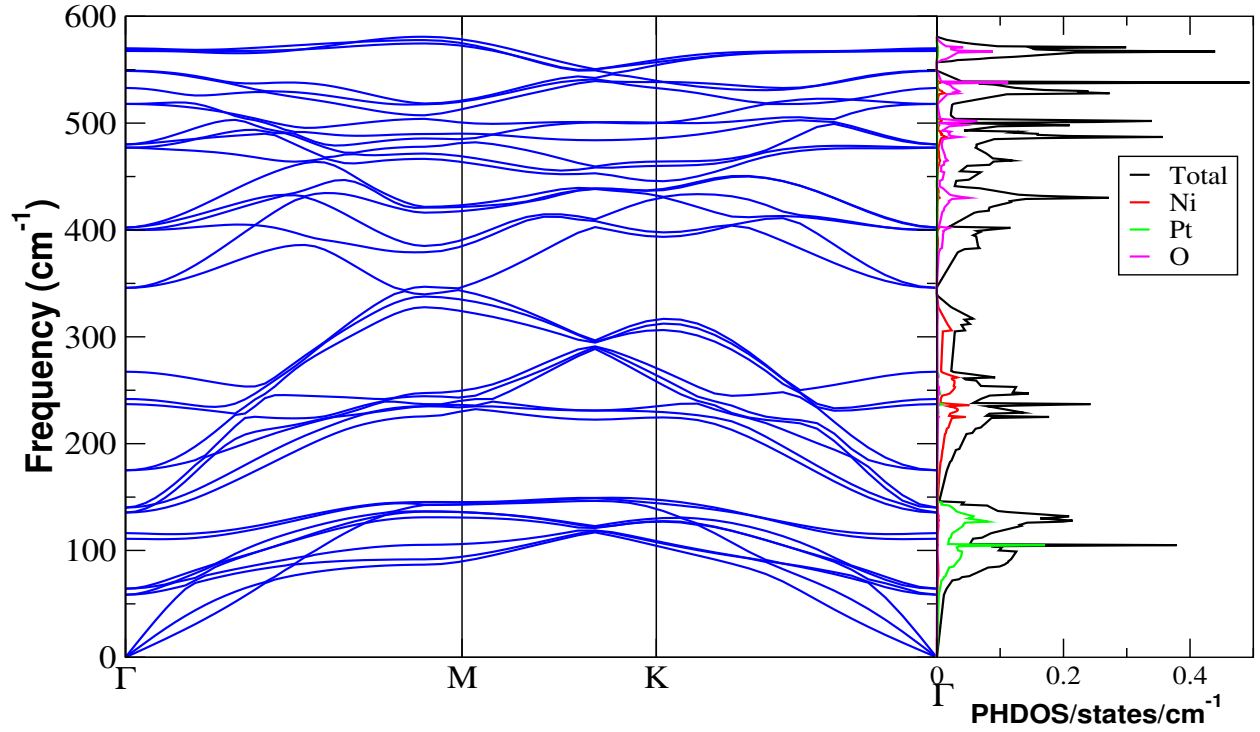


Figure 2: Calculated phonon spectrum of PtNiO₂

major contribution of O and minor contribution of Ni in higher optical modes whereas the middle optical modes are mainly due to O. The frequencies of the acoustic phonon branches are in an interval of 0 up to 110 cm⁻¹, with an overlap with optical phonon modes of

low frequencies. The higher optical modes are less dispersive than optical modes at lower and middle regions which represents strong intra-molecular interactions. At high symmetry point M, O atom vibrate with frequency 581 cm^{-1} , which is maximum frequency of vibration. The real phonon spectrum shown Fig. 2 ensures the dynamical stability of the system and provides an insight for experimental realization.

Electronic and magnetic properties

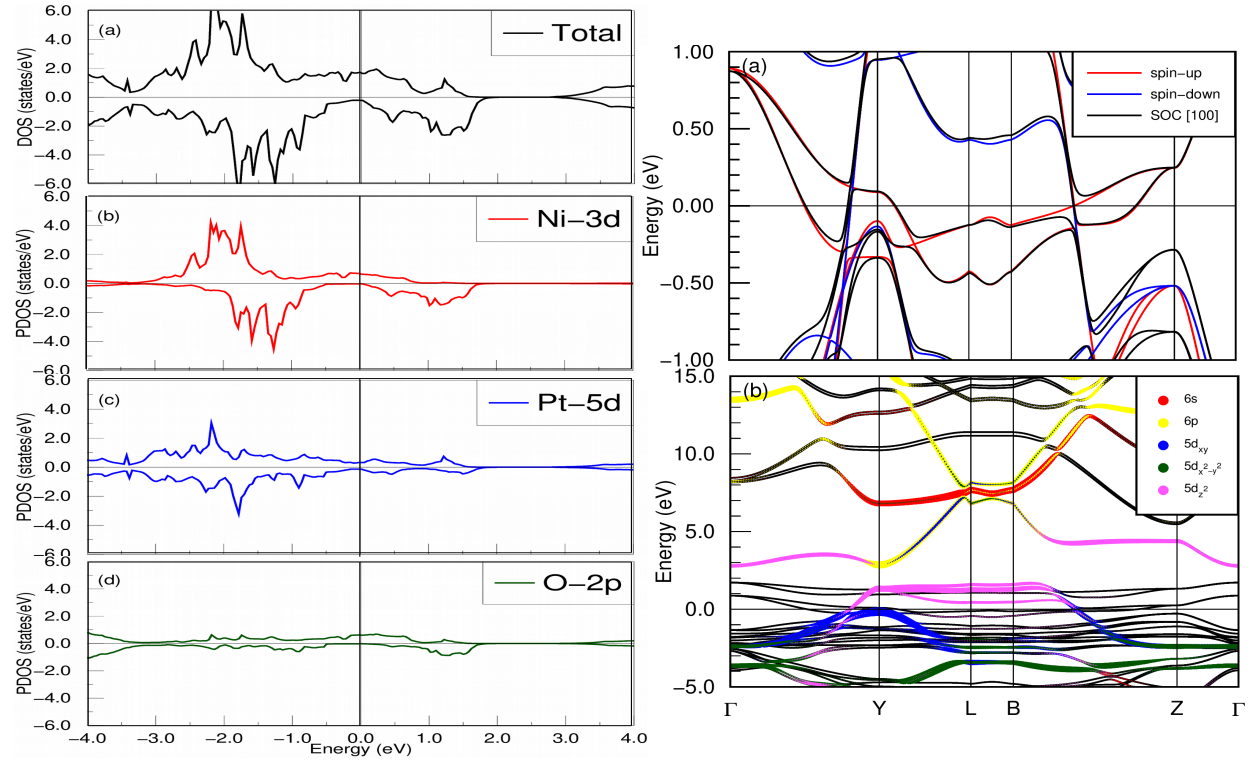


Figure 3: Left: (a-d) Total and partial DOS in scalar relativistic mode. The spin-up and spin-down components are located on the upper and lower parts respectively. Right: (a) Electronic band structures of PtNiO₂ without and with SOC (easy anisotropy along [100] direction). Red and blue color represent the spin up and down bands respectively. (b) Orbital characteristics analysis of Pt *s*, *p* and *d* orbitals.

Similar to most of the 3R delafossites, Pt takes the charge state +1. The outermost orbital of it contains *d* orbital characters, with $5d^9$ configuration. The transition metal normally is in +3 oxidation state with $3d^7$ configuration, lying mostly in valence band region as observed in Fig. 3(b). O-2*p* states consisting of four electrons in the *p* orbitals have

dominant contribution around the E_F . Electronic structure shown in Fig. 3(a) supports that PtNiO₂ is metallic in nature due to the presence of significant density of states (DOS) around the E_F . From our total energy calculation for non-magnetic (NM), ferro-magnetic (FM) and ferri-magnetic (FIM) configurations, ground state is found to be FM ($\uparrow\uparrow$) with the lowest energy. The calculated effective magnetic moments per unit cell is $1.01 \mu_B$.

To determine the magnetic easy axis, the full-relativistic total energies are computed along magnetization axis [001] and [100], respectively. Magnetic easy axis was found along the [100] magnetization direction with magnetic anisotropic energy of 62 meV per unit cell.

Electronic properties of PtNiO₂ resembles with its sister compound PtCoO₂ reported earlier.³⁷ Co has six electrons on its d orbital. Crystal field due to oxygen octahedron splits Co d subshell into lower t_{2g} and higher e_g orbital, resulting in the configuration $t_{2g}^{3\uparrow}e_g^{0\uparrow}t_{2g}^{3\downarrow}e_g^{0\downarrow}$. With the fully occupied t_{2g} orbitals, all the magnetic moment cancels in PtCoO₂ whereas in PtNiO₂, Ni has an additional spin up electron in e_g orbital following the Hund's rule resulting in $t_{2g}^{3\uparrow}e_g^{1\uparrow}t_{2g}^{3\downarrow}e_g^{0\downarrow}$. This renders $1 \mu_B$ magnetic moment in an ionic picture, in agreement with our DFT calculations. The NiO₆ octahedron pushes spin-up channel away from the E_F , resulting on large exchange energy (≈ 1 eV) [Fig. 3(a) right panel]. Pt forms a triangular lattice in PtNiO₂. Pt $5d_{z^2}$ orbitals contribute to the conduction as depicted in [Fig. 3(b) right panel]. High conductivity of PtNiO₂ is possible due to the triangular lattice layer of Pt, where each Pt has a free electron,^{37,44} as it's sister compound PtCoO₂.

The special feature realized in a kagome-like electronic structure is a quadratic band crossing between dispersive and non-dispersive band at Γ .^{45–47} Quadratic band crossing points are protected by time-reversal and C_4 or C_6 rotational symmetries in different lattice models.⁴⁶ In kagome system, it is protected by time-reversal and C_6 rotational symmetry.⁴⁵ Quadratic band dispersion are even realized in magnetic semi-metals.⁴⁸ At K high symmetry point, Pt $s+p_x/p_y$ and Pt $3d_{z^2-r^2} + d_{xy}/d_{x^2-y^2}$ formed a nearly three-fold degeneracy, yielding PtCoO₂, a kagome system hidden in the triangular lattice. The sharp band crossing the E_F has mainly the d orbital character with hidden combination of $s+p_x/p_y$,³⁷ which

renders the high conductivity to PtCoO₂. Similar to this, for PtNiO₂, orbital analysis of Pt (*s*, *p* and *d* orbital) reveals a quadratic band crossing of a flat band and a dispersive band at Γ , touching at around 8 eV above the E_F (see Fig. 3(b) right panel). It shows that Pt *s*, *p* orbitals forms a kagome-like electronic structure much above the E_F . Such system with kagome-like structure exhibits a (near) three fold degeneracy at K-point similar to PtCoO₂.³⁷ This degenerate point is at around 8 eV above the E_F , in PtNiO₂, representing our system as a hidden kagome-like system. This system provides a platform to understand the interplay of magnetism, hidden kagome-like lattice and Weyl fermions.

Weyl properties with SOC

Electronic band structure of PtNiO₂ without and with SOC is shown in [Fig. 3(a) right panel]. It can be noted that a number of bands cross each other at E_F . Crystal field is found to split Pt in three energy states. The conduction band belonging to 2D E irreducible representation forms a crossing near high symmetry point Y slightly above E_F . This degenerate band at Γ splits due to reduction in symmetry along the line Γ -Y. Along the Γ -Y and B-Z lines at the E_F , we observe band inversion as well as band crossing. With SOC taken into account, the band structure around the E_F changes considerably. A significant band gap opening has been observed. The effect of SOC indicates the topological characteristics of the material. Band gap opening are noted between Γ -Y and B-Z region in the band structure. Effect of SOC results in the interactions between band topology and materials magnetism. Basing on these observation, we further explore the Weyl features. WPs has been computed for the magnetization easy axis [100], wherein 20 pairs of WPs are found. Table 1 lists their energies, multiplicity, chirality, and location of WPs within 100 meV above the E_F . As the location of WPs are close to E_F , their identification may be possible from transport experiment. Fig. 4 shows the distribution of WPs in 2D first BZ. Pairs of W_2 and W_3 's Weyl points are connected by M_y . Due to such WPs identification this system has possibilities for large intrinsic anomalous Hall conductivity due to the large Berry curvature

because large Berry curvature comes from the monopole of Weyl points. In full relativistic mode (i.e. SOC), Fermi surface spectral functions have been investigated. Right of Fig. 4 shows the Fermi surface spectral function for a semi infinite slab in the k_x and k_y plane.

Our Fermi surface spectral function calculation confirmed that PtNiO_2 has a hidden kagome-like lattice structure.

Table 1: Characteristics of Weyl points in the PtNiO_2 electronic structure, when the magnetization along $[100]$ direction. There are four sets of Weyl nodes. Within each set, the representative k_i ($i = x, y, z$) positions are also given, in units of \AA^{-1}

WP	Energy(meV)	Multiplicity	k_x	k_y	k_z	χ
W_1	24	4	-0.327	0.221	0.114	-1.0
W_2	88	2	-0.234	-0.000	-1.029	-1.0
W_3	95	2	-0.452	0.000	-0.512	1.0
W_4	98	4	-0.108	0.189	1.074	-1.0

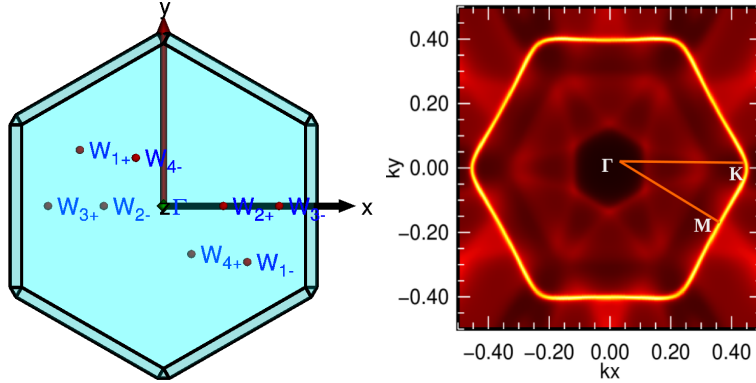


Figure 4: Left: Distribution of Weyl points in first 2D BZ. Right: Fermi surface spectral function.

Conclusions

In conclusions, using density functional theory we investigated the electronic, magnetic and Weyl features of PtNiO_2 . The identification of 20 pairs of confirmed Weyl points along the easy axis $[100]$ close to Fermi level deserves the experimental work. The change in magnetization direction of PtNiO_2 breaks the specified symmetries, resulting change in the

number of Weyl points. Furthermore, PtNiO_2 is found to be a 2D hidden kagome-like lattice. Our findings suggest that PtNiO_2 could be a viable platform for studying the interaction between topological properties and magnetism. They also provide a good material base for future transport and surface studies in delafossites.

Acknowledgement

The author thanks M. Richter (IFW-Dresden) and Rajendra Adhikari (Kathmandu University) for fruitful discussions. This work was funded by the University Grants Commission (UGC) Nepal, through award number CRG-78/79-S&T-03. M.B.N. and R.G. are supported by UGC-Nepal. G.B.A. thanks Nepal Academy of Science and Technology for the PhD fellowship. M.P.G. and G.B.A. thanks Ulrike Nitzsche for the technical assistance.

References

- (1) Armitage, N. P.; Mele, E. J.; Vishwanath, A. *Rev. Mod. Phys.* **2018**, *90*, 015001.
- (2) Xia, B. W.; Jin, Y. J.; Zhao, J. Z.; Chen, Z. J.; Zheng, B. B.; Zhao, Y. J.; Wang, R.; Xu, H. *Phys. Rev. Lett.* **2019**, *122*, 057205.
- (3) Wang, Z.; Sun, Y.; Chen, X.-Q.; Franchini, C.; Xu, G.; Weng, H.; Dai, X.; Fang, Z. *Phys. Rev. B* **2012**, *85*, 195320.
- (4) Liu, Z. K.; Zhou, B.; Zhang, Y.; Wang, Z. J.; Weng, H. M.; Prabhakaran, D.; Mo, S.-K.; Shen, Z. X.; Fang, Z.; Dai, X.; Hussain, Z.; Chen, Y. L. *Science* **2014**, *343*, 864–867.
- (5) Wan, X.; Turner, A. M.; Vishwanath, A.; Savrasov, S. Y. *Phys. Rev. B* **2011**, *83*, 205101.
- (6) Burkov, A. A.; Balents, L. *Phys. Rev. Lett.* **2011**, *107*, 127205.

- (7) Xu, G.; Weng, H.; Wang, Z.; Dai, X.; Fang, Z. *Phys. Rev. Lett.* **2011**, *107*, 186806.
- (8) Xu, Y.; Zhang, F.; Zhang, C. *Phys. Rev. Lett.* **2015**, *115*, 265304.
- (9) Soluyanov, A. A.; Gresch, D.; Wang, Z.; Wu, Q.; Troyer, M.; Dai, X.; Bernevig, B. A. *Nature* **2015**, *527*, 495–498.
- (10) Burkov, A. A.; Hook, M. D.; Balents, L. *Phys. Rev. B* **2011**, *84*, 235126.
- (11) Zhu, Z.; Winkler, G. W.; Wu, Q.; Li, J.; Soluyanov, A. A. *Phys. Rev. X* **2016**, *6*, 031003.
- (12) Winkler, G. W.; Singh, S.; Soluyanov, A. A. *Chin. Phys. B* **2019**, *28*, 077303.
- (13) Yan, B. *Science China Physics, Mechanics, and Astronomy* **2021**, *64*, 217063.
- (14) Shekhar, C. et al. *Nat. Phys.* **2015**, *11*, 645–649.
- (15) Kumar, N. et al. *Nature Communications* **2017**, *8*, 1642.
- (16) Thakur, G. S.; Vir, P.; Guin, S. N.; Shekhar, C.; Weihrich, R.; Sun, Y.; Kumar, N.; Felser, C. *Chem. Mater.* **2020**, *32*, 1612–1617, PMID: 32116410.
- (17) Hosur, P.; Qi, X. *C R Phys* **2013**, *14*, 857–870.
- (18) Morimoto, T.; Zhong, S.; Orenstein, J.; Moore, J. E. *Phys. Rev. B* **2016**, *94*, 245121.
- (19) Zyuzin, A. A.; Zyuzin, A. Y. *Phys. Rev. B* **2017**, *95*, 085127.
- (20) Sirica, N. et al. *Phys. Rev. Lett.* **2019**, *122*, 197401.
- (21) Liu, E. et al. *Nat. Phys.* **2018**, *14*, 1125–1131.
- (22) Wang, Q.; Xu, Y.; Lou, R.; Liu, Z.; Li, M.; Huang, Y.; Shen, D.; Weng, H.; Wang, S.; Lei, H. *Nature communications* **2018**, *9*, 3681.
- (23) Liu, D. F. et al. *Science* **2019**, *365*, 1282–1285.

- (24) Ghimire, M. P.; Facio, J. I.; You, J.-S.; Ye, L.; Checkelsky, J. G.; Fang, S.; Kaxiras, E.; Richter, M.; van den Brink, J. *Phys. Rev. Research* **2019**, *1*, 032044.
- (25) Sakai, A.; Mizuta, Y. P.; Nugroho, A. A.; Sihombing, R.; Koretsune, T.; Suzuki, M.-T.; Takemori, N.; Ishii, R.; Nishio-Hamane, D.; Arita, R.; Goswami, P.; Nakatsuji, S. *Nat. Phys.* **2018**, *14*, 1119–1124.
- (26) Guin, S. N.; Manna, K.; Noky, J.; Watzman, S. J.; Fu, C.; Kumar, N.; Schnelle, W.; Shekhar, C.; Sun, Y.; Gooth, J.; Felser, C. *NPG Asia Materials* **2019**, *11*, 16.
- (27) Kübler, J.; Felser, C. *EPL (Europhysics Letters)* **2016**, *114*, 47005.
- (28) Kuroda, K. et al. *Nat. Mater.* **2017**, *16*, 1090–1095.
- (29) Yang, H.; Sun, Y.; Zhang, Y.; Shi, W.-J.; Parkin, S. S. P.; Yan, B. *New J. Phys.* **2017**, *19*, 015008.
- (30) Hirschberger, M.; Kushwaha, S.; Wang, Z.; Gibson, Q.; Liang, S.; Belvin, C. A.; Bernevig, B. A.; Cava, R. J.; Ong, N. P. *Nat. Mater.* **2016**, *15*, 1161–1165.
- (31) Borisenko, S.; Evtushinsky, D.; Gibson, Q.; Yaresko, A.; Koepernik, K.; Kim, T.; Ali, M.; van den Brink, J.; Hoesch, M.; Fedorov, A.; Haubold, E.; Kushnirenko, Y.; Soldatov, I.; Schäfer, R.; Cava, R. J. *Nature communications* **2019**, *10*, 3424.
- (32) Shannon, R. D.; Rogers, D. B.; Prewitt, C. T. *Inorg. Chem.* **1971**, *10*, 713–718.
- (33) Kushwaha, P.; Sunko, V.; Moll, P. J. W.; Bawden, L.; Riley, J. M.; Nandi, N.; Rosner, H.; Schmidt, M. P.; Arnold, F.; Hassinger, E.; Kim, T. K.; Hoesch, M.; Mackenzie, A. P.; King, P. D. C. *Sci. Adv.* **2015**, *1*, e1500692.
- (34) Shannon, R. D.; Rogers, D. B.; Prewitt, C. T.; Gillson, J. L. *Inorg. Chem.* **1971**, *10*, 723–727.

- (35) Cerqueira, T. F. T. Structural prediction and materials design from high throughput to global minima optimization methods. Ph.D. thesis, 2018.
- (36) Daou, R.; Frésard, R.; Eyert, V.; Hébert, S.; Maignan, A. *Science and Technology of Advanced Materials* **2017**, *18*, 919–938.
- (37) Usui, H.; Ochi, M.; Kitamura, S.; Oka, T.; Ogura, D.; Rosner, H.; Haverkort, M. W.; Sunko, V.; King, P. D. C.; Mackenzie, A. P.; Kuroki, K. *Phys. Rev. Materials* **2019**, *3*, 045002.
- (38) Zhang, C. et al. *Nat. Mater.* **2019**, *18*, 482–488.
- (39) Koepnick, K.; Eschrig, H. *Phys. Rev. B* **1999**, *59*, 1743–1757.
- (40) Perdew, J. P.; Burke, K.; Ernzerhof, M. *Phys. Rev. Lett.* **1996**, *77*, 3865–3868.
- (41) Giannozzi, P. et al. *Journal of Physics: Condensed Matter* **2009**, *21*, 395502.
- (42) Smidstrup, S.; Stradi, D.; Wellendorff, J.; Khomyakov, P. A.; Vej-Hansen, U. G.; Lee, M.-E.; Ghosh, T.; Jónsson, E.; Jónsson, H.; Stokbro, K. *Phys. Rev. B* **2017**, *96*, 195309.
- (43) Jain, A.; Ong, S. P.; Hautier, G.; Chen, W.; Richards, W. D.; Dacek, S.; Cholia, S.; Gunter, D.; Skinner, D.; Ceder, G.; Persson, K. A. *APL materials* **2013**, *1*, 011002.
- (44) Eyert, V.; Frésard, R.; Maignan, A. *Chem. Mater.* **2008**, *20*, 2370–2373.
- (45) Du, L.; Zhou, X.; Fiete, G. A. *Phys. Rev. B* **2017**, *95*, 035136.
- (46) Sun, K.; Yao, H.; Fradkin, E.; Kivelson, S. A. *Phys. Rev. Lett.* **2009**, *103*, 046811.
- (47) Kang, M.; Fang, S.; Ye, L.; Po, H. C.; Denlinger, J.; Jozwiak, C.; Bostwick, A.; Rotenberg, E.; Kaxiras, E.; Checkelsky, J. G.; Comin, R. *Nat. Commun.* **2020**, *11*, 4004.
- (48) Fang, C.; Gilbert, M. J.; Dai, X.; Bernevig, B. A. *Phys. Rev. Lett.* **2012**, *108*, 266802.